Evaluation of emission contributions from charge-exchange between the excited states of deuterium with He$^+$ during diagnostic of thermal helium gas beam injection and laser-induced fluorescence

J. M. Muñoz Burgos,[1, a)] M. Griener,[2, b)] J. Loreau,[3, c)] A. Gorbunov,[4, d)] T. Lunt,[2, e)] O. Schmitz,[5, f)] and E. Wolfrum[2, g)]

[1)] *Astro Fusion Spectre, LLC, San Diego, CA 92127, USA*

[2)] *Max Planck Institute for Plasma Physics, Boltzmannstr. 2, D-85748 Garching, Germany*

[3)] *Service de Chimie Quantique et Photophysique, Universite Libre de Bruxelles (ULB) CP 160/09, 1050 Brussels, Belgium*

[4)] *National Research Center Kurchatov Institute, Akademika Kurchatova sq. 1, 123182 Moscow, Russia*

[5)] *Department of Engineering Physics, University of Wisconsin - Madison, Madison, WI 53706, USA*

(Dated: 20 May 2019)

Emission contributions from charge-exchange of excited deuterium (n = 2, 3) with He$^+$ are evaluated in a 1-D kinetic collisional radiative model (CRM) in order to analyze their effects on the Thermal Helium Beam (THB) line-ratio diagnostic on ASDEX Upgrade (AUG), and Laser Induced Fluorescence (LIF) He I density measurements in ITER. Recent charge-exchange calculations show that cross-sections from excited deuterium (n = 2, 3) with He$^+$ are over 4-orders of magnitude higher than those from the ground state (n = 1), and occur at very low energies where they are more likely to interact with the thermal He$^+$ ions introduced by ionization of the diagnostic helium gas-puff injection. Higher densities of excited deuterium are typically present in the Scrape-Off Layer (SOL), Divertor, and Edge regions of Tokamaks, where the LIF and THB helium diagnostic are typically used for n_{HeI} and simultaneous determination of electron temperatures and densities, and where contributions from charge-exchange emission may offset these values if not taken into account. The analysis presented in this work shows that due to the higher density of deuterium in the ground rather than in excited states, and the divergent behavior of deuterium and He$^+$ density profiles along the SOL and Edge regions, the deuterium-He$^+$ charge-exchange contributions to the helium puff emission are 3-orders of magnitude lower than those from electron-impact excitation. Similar plasma conditions are expected in the ITER divertor, with the exception that in the area near the strike-points and targets the electron temperature is not high enough to excite from the ground state but, deuterium, electron, and He$^+$ densities are high enough to dominate the emission from charge-exchange and recombination. These findings strengthen the assumption made in the present line-ratio model that helium emission from gas-puff into plasma is mainly dominated byelectron-excitation. It is also shown that in general, charge-exchange helium emission is 2-orders of magnitude higher than emission due to recombination. These findings suggest the importance of including charge-exchange processes as a source of neutrals in ionic fractional abundance calculations in plasmas, and helium-ash transport modeling in fusion reactors.

I. INTRODUCTION

Determination of electron temperatures and densities using line-ratio spectroscopy on locally injected thermal helium has been applied in a variety fusion devices such as tokamaks and stellarators.[1–3] The challenge of large relaxation times of the metastable state of helium intrinsic in this powerful diagnostic has been addressed by the inclusion of time-dependent collisional radiative models.[4,5] Recently the THB diagnostic has been upgraded at AUG[2,6] to allow measurements of high temporal and spatial resolution electron temperature and density profiles. This high temporal and spatial resolution capability covers both the plasma edge and SOL regions, and allows for determination of critical transport quantities with resolution of turbulent structures, filaments, and single Edge Localized Modes (ELMs).[2]

In an effort to continue testing and validating this powerful diagnostic, forward modeling of helium beam gas-puff using a 1-D kinetic collisional radiative model, as well as other synthetic analysis have been previously developed.[7,8] In that model, additional atomic processes present in the edge and SOL regions plasma conditions such as proton ionization and proton-helium charge-exchange have been included.[9]

---

a)Electronic mail: astrofusionspectre@gmail.com.

b)Electronic mail: michael.griener@ipp.mpg.de.

c)Electronic mail: jloreau@ulb.ac.be.

d)Electronic mail: alexeygor@mail.ru.

e)Electronic mail: tilmann.lunt@ipp.mpg.de.

f)Electronic mail: oschmitz@wisc.edu.

g)Electronic mail: Elisabeth.Wolfrum@ipp.mpg.de.

The forward 1-D kinetic model revealed that elect impact excitation and ionization are the dominating lisional mechanisms during the emission and deple of the helium neutral gas as injected for diagnostic poses. It also showed that interactions between the tral helium in the gas-puff and protons were severa ders of magnitude lower with respect to interactions electrons, therefore validating the reliability of this erful diagnostic tool.[4,7]

Recent atomic charge-exchange (CX) calculations excited hydrogen isotopes with He^+ ions suggest additional emission from recently formed helium trals may have to be taken into account in the ratio calculation to obtain accurate electron densities temperatures.[10] Excited hydrogen ($n = 2, 3$) with CX cross-sections are over 4-orders of magnitude hi than CX from the ground state ($n = 1$).[10–12] This process also occurs at lower energies where interact between recently formed low temperature helium ions and hydrogen isotopes is more likely to occur, particularly in the edge and SOL regions.

LIF diagnostic is based on interaction of the laser radiation with plasma and observation of the response signals (fluorescence). The laser excites allowed transitions of atoms or ions temporally increasing emission in the pumping and other lines. Fluorescent signals depend on the local density as well as, laser parameters and excitation processes such as electron-impact excitation, recombination, and charge-exchange. LIF on ITER will be used to measure neutral helium densities (n_{HeI}) in the outer leg of the divertor, where high gradients of plasma parameters are expected ($T_e = 0.3 - 200 \, eV$, $n_D = 10^9 - 10^{15} \, cm^{-3}$, $n_{HeI} = 10^9 - 10^{13} \, cm^{-3}$, and $n_{HeII} = 10^9 - 5 \times 10^{12} \, cm^{-3}$). Therefore, deuterium/electron-He^+ CX/recombination emission may be dominant versus electron-excitation in some spatial points. CX complicate fluorescent signal interpretation to determine n_{HeI} density values as additional information about n_D and n_{HeII} densities is needed, when electron densities and temperatures are obtained from the ITER divertor Thomson scattering diagnostic to consider only electron-impact processes.[13]

The additional populating CX mechanism for the two spin systems of helium is illustrated in figure 1. The repopulation of neutral helium by CX is different for the singlet and triplet systems. These differences influence the line-ratios, and thus the temperature and density values that are calculated. The fluorescent signal from helium neutrals are also a function of the initial population in both ground (1^1S) and metastable states (2^1S and 2^3S), therefore CX populating mechanisms of these states affect the LIF n_{HeI} density measurements.

In order to quantify the emission from recently formed neutral helium by CX and compare it to the bulk gas-puff emission, the previously developed 1-D kinetic CRM is expanded to include both deuterium CX, as well as electron recombination with He^+ ions.[7]
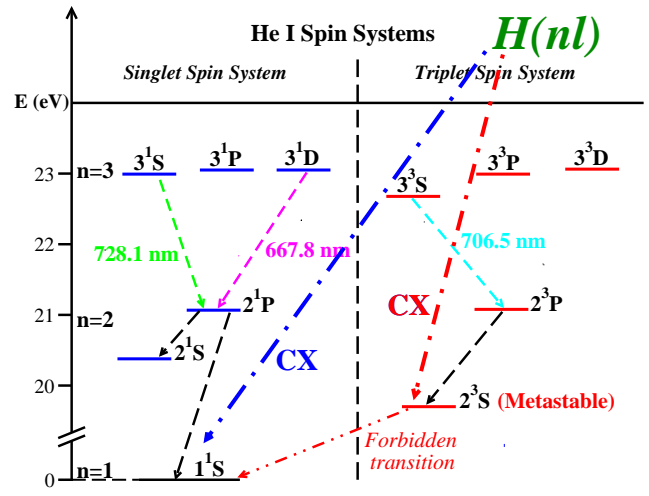
The model includes the same state-of-the-art R-

FIG. 1. Grotrian diagram showing the hydrogen-He^+ charge-exchange process for both, singlet (^1S ground state), and triplet (^3S metastable state) spin systems of helium.[7]

Matrix,[14] R-Matrix With Pseudo-States (RMPS)[15] electron excitation data used in the previous model.[7] The tabulated/interpolated temperature-dependent electron-ionization rate-coefficients have been replaced by numerically calculated values each time the model is run. The model uses Convergent Close Coupling (CCC) ionization cross-sections,[16,17] which are used to calculate Maxwellian rate-coefficients.[5,18] The atomic data set of the Hibrid-Time-Dependent/Independent (HTD/I) helium line-ratio model has also been updated with the same ionization CCC data.[4]

The first part of this paper describes the newly calculated set of deuterium-He^+ CX cross-sections and their implementation on the 1-D kinetic CRM solution, as well as the inclusion of electron recombination into the model.

In the second part of this paper, the 1-D model is used to calculate emissivities along the center of propagation of a simulated gas-puff using plasma profiles from AUG. In order to quantify the CX emission contributions from excited states of deuterium, the population of these states must be known. A quasi-static equilibrium CRM model is employed to calculate the population density of excited states of the local deuterium using plasma profiles from AUG. The CX emission is then compared to those from electron-recombination and electron excitation in the helium puff.

In the third part, a brief description of the LIF diagnostic at ITER is presented. The collisional radiative model is used to quantify contributions of CX and recombination to initial 2^1S and 2^3S state populations from where the laser photo-excitation ocurrs using plasma parameters provided by SOLPS calculations.

II. KINETIC COLLISIONAL RADIATIVE MODEL

The mathematical solution is expanded from the already developed 1-D kinetic CRM model.[7] For the following derivation, ion-impact ionization and He-proton CX are ignored since it has been shown that those depletion mechanisms are many orders of magnitude lower than electron ionization.[7] The solution now includes additional populating mechanisms for each of the nl atomic terms:

- Radiative decay: $[A_{ml' \to nl}/A_{nl \to ml'}]$

- Electron-impact excitation/de-excitation:
$$[q^e_{ml' \to nl}/\ q^e_{nl \to ml'}]$$

- Electron-impact ionization: $[S^e_{nl}]$

- Deuterium-He$^+$ charge-exchange: $[\sigma^{CX_D}_{nl}]$

- Radiative recombination: $[\alpha^{(r)}_{nl}]$

- Dielectronic recombination: $[\alpha^{(d)}_{nl}]$

- Three-body recombination: $[\alpha^{(3)}_{nl}]$

The excited deuterium ($n = 2, 3$)-He$^+$ CX cross-sections for each of the two spin systems of helium have been recently calculated.[10] Including the channels for each of the spin systems is very important to take into account when modeling helium emission due to the long relaxation times of the metastable (See figure 1). In this work, only the cross-sections for deuterium were used since it is the main isotope used in AUG and in many other research reactors. It was found that there are small isotopic differences in the cross-sections between hydrogen, deuterium, and tritium, particularly in the low collision energy region.[10]

The cross-sections for both spin systems of helium are shown in figure 2.

The neutral atoms interacting with a plasma populating the excited nl-term state are described using the kinetic equation that includes the atomic collisional processes on the right hand side:[7]

$$\frac{\partial f_{nl}}{\partial t} + \boldsymbol{v} \cdot \nabla f_{nl} = \sum_{nl \neq ml'} \left[A_{ml' \to nl} + n_e q^e_{ml' \to nl} \right] f_{ml'}$$

$$- \left\{ n_e S^e_{nl} + \sum_{nl \neq ml'} \left[A_{nl \to ml'} + n_e q^e_{nl \to ml'} \right] \right\} f_{nl}$$

$$+ \left\{ n_D q^{CX_D}_{nl}(\boldsymbol{v}) + n_e \left[\alpha^{(r)}_{nl} + \alpha^d_{nl} + n_e \alpha^{(3)}_{nl} \right] \right\} f_{He^+}(\boldsymbol{v}) , \quad (1)$$

where n_e and n_D are the free electron/deuterium densities, and $f_{nl}(\boldsymbol{v}, \boldsymbol{r}, t)$ is the neutral atom distribution function in the excited nl-term. The deuterium-He$^+$ CX rate-coefficient is described by

$$q^{CX_D}_{nl}(\boldsymbol{v}) = \frac{1}{n_D} \int d^3\boldsymbol{v}' |\boldsymbol{v} - \boldsymbol{v}'| \sigma^{CX_D}_{nl}(|\boldsymbol{v} - \boldsymbol{v}'|) f_D(\boldsymbol{v}') , \quad (2)$$

with deuterium and He$^+$ distribution functions:

$$f_D(\boldsymbol{v}) = \frac{n_D}{\pi^{3/2} v^3_{th_D}} e^{-\boldsymbol{v}^2/v^2_{th_D}}$$

$$f_{He^+}(\boldsymbol{v}) = \frac{n_{He^+}}{\pi^{3/2} v^3_{th_{He^+}}} e^{-\boldsymbol{v}^2/v^2_{th_{He^+}}} , \quad (3)$$

and a thermal velocities:

$$v_{th_D} = \sqrt{\frac{2k_B T_D}{m_D}}$$

$$v_{th_{He^+}} = \sqrt{\frac{2k_B T_{He^+}}{m_{He^+}}} . \quad (4)$$

The solution to the kinetic equation is assumed to be in the form:[7]

$$f_{nl}(\boldsymbol{v}, \boldsymbol{r}, t) = f_o(\boldsymbol{v}) n_{nl}(\boldsymbol{r}, t) , \quad (5)$$

with the density of the nl-state population $n_{nl}(\boldsymbol{r}, t)$, a shifted flow velocity defined as: $v_n = M\sqrt{\gamma k_B T_n/m_n}$, where M is the Mach number, T_n is the temperature,
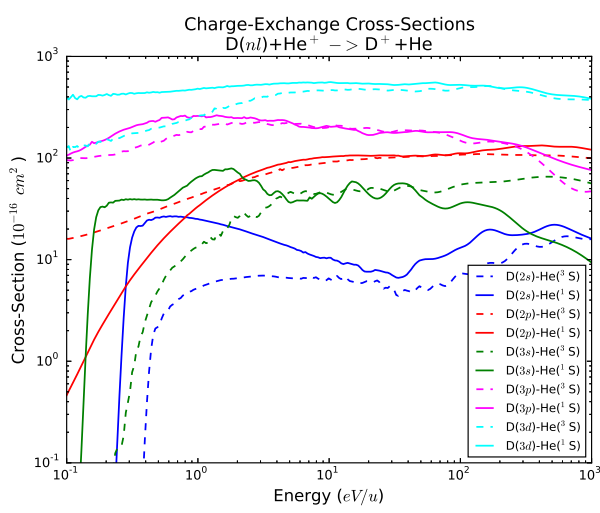
FIG. 2. Charge-exchange cross-sections between deuterium and He$^+$ for the two spin systems of helium: D(nl)+He$^+$ → D$^+$+He(^{1}S,^{3}S). Recent calculations have shown that there are isotopic differences in the cross-sections between; hydrogen, deuterium, and tritium, particularly at the lower limit of collision energies.[10]

and m_n is the mass of the neutrals, and $\gamma = 5/3$ for helium.[7,19]:

$$f_o(\boldsymbol{v}) = \frac{1}{\pi^{3/2} v_{th_n}^3} e^{-(\boldsymbol{v}-\boldsymbol{v_n})^2/v_{th_n}^2} \ . \tag{6}$$

Equation (1) is integrated with respect to velocity to obtain:[7]

$$\frac{\partial n_{nl}}{\partial t} + \boldsymbol{v_n} \cdot \nabla n_{nl} = \sum_{nl \neq ml'} \left[A_{ml' \to nl} + n_e q^e_{ml' \to nl} \right] n_{ml'}$$

$$- \left\{ n_e S^e_{nl} + \sum_{nl \neq ml'} \left[A_{nl \to ml'} + n_e q^e_{nl \to ml'} \right] \right\} n_{nl}$$

$$+ n_D \int d^3 \boldsymbol{v} q_{nl}^{CX_D}(\boldsymbol{v}) f_{He^+}(\boldsymbol{v}) + n_e n_{He^+} \left[\alpha^{(r)}_{nl} + \alpha^d_{nl} + n_e \alpha^{(3)}_{nl} \right] \ . \tag{7}$$

Using the definition of deuterium-He$^+$ CX rate-coefficient from equation (2), the generalized CX coefficients ($Q_{nl}^{CX_D}$) are defined as:

$$n_D \int d^3 \boldsymbol{v} q_{nl}^{CX_D}(\boldsymbol{v}) f_{He^+}(\boldsymbol{v}) = n_D n_{He^+} Q_{nl}^{CX_D} \ . \tag{8}$$

The generalized CX rate-coefficient is numerically integrated from[7]

$$Q_{nl}^{CX_D} = \frac{4}{\sqrt{\pi}} \sqrt{v_{th_D}^2 + v_{th_{He^+}}^2} \int_0^\infty d\nu \nu^3 \sigma_{nl}^{CX_D}(\nu) e^{-\nu^2} \ , \tag{9}$$

where the non-dimensional quantity ν is defined as a function of the center of mass energy between the deu-

terium and He$^+$:

$$\nu = \frac{1}{\sqrt{v_{th_D}^2 + v_{th_{He^+}}^2}} \sqrt{\frac{2eE(eV/u)}{m_u}} \ . \tag{10}$$

Figure 3 shows the numerically calculated generalized rate-coefficients using equation (9), the cross-sections shown in figure 2, and Gauss-Laguerre Quadrature.[20] The ion temperature $T_{He^+} = 300K$ was chosen under the assumption that once the helium puff gets ionized, it does not have enough time to be thermalized by elastic collisions before either recombining or receiving an electron through CX. However, the He$^+$ temperature was varied and showed little change from these values.

Choosing the propagation velocity axis of the gas-puff along the radial direction $\boldsymbol{v_n} = v_n \hat{\boldsymbol{r}}$, equation (7) is expressed as:
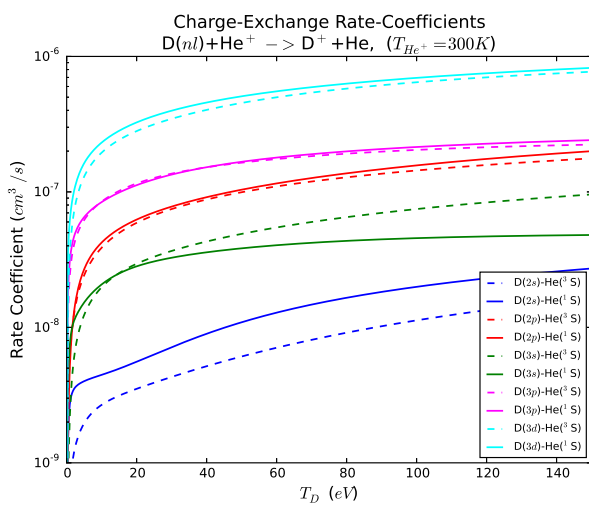
FIG. 3. Generalized charge-exchange rate-coefficients for the two spin systems of helium [D(nl)+He$^+$ → D$^+$+He(^{1}S,^{3}S)] calculated using equation (9), and $T_{He^+} = 300K$.[10]

$$\frac{\partial n_{nl}}{\partial t} + v_n \frac{\partial n_{nl}}{\partial r} = \sum_{nl \neq ml'} \left[A_{ml' \to nl} + n_e q^e_{ml' \to nl} \right] n_{ml'}$$

$$- \left\{ n_e S^e_{nl} + \sum_{nl \neq ml'} \left[A_{nl \to ml'} + n_e q^e_{nl \to ml'} \right] \right\} n_{nl}$$

$$+ n_{He^+} \left\{ n_D Q^{CX_D}_{nl} + n_e \left[\alpha^{(r)}_{nl} + \alpha^d_{nl} + n_e \alpha^{(3)}_{nl} \right] \right\} , \qquad (11)$$

that can now be written in terms of the collisional radiative matrix and the charge-exchange/recombination coefficients:

$$\frac{\partial n_{nl}}{\partial t} + v_n \frac{\partial n_{nl}}{\partial r} = \sum_{nl \neq ml'} C_{nl,ml'} n_{ml'} + C_{nl,nl} n_{nl} + n_{He^+} R^{CX_D,r}_{nl} . \qquad (12)$$

The non-diagonal elements of the matrix (gains) are represented by

$$C_{nl,ml'} = A_{ml' \to nl} + n_e q^e_{ml' \to nl} , \qquad (13)$$

and the diagonal elements (losses) by

$$C_{nl,nl} = - \left\{ n_e S^e_{nl} \right.$$

$$\left. + \sum_{nl \neq ml'} \left[A_{nl \to ml'} + n_e q^e_{nl \to ml'} \right] \right\} . \qquad (14)$$

The charge-exchange/recombination coefficients are defined as

$$R^{CX_D,r}_{nl} = n_D Q^{CX_D}_{nl} + n_e \left[\alpha^{(r)}_{nl} + \alpha^d_{nl} + n_e \alpha^{(3)}_{nl} \right] . \qquad (15)$$

$$\frac{dn_{nl}}{ds} = \sum_{nl \neq ml'} C_{nl,ml'} n_{ml'} + C_{nl,nl} n_{nl} + n_{He^+} R_{nl}^{CX_D,r} \,.$$

(16)

Using the method of integration along characteristics,[7] equation (11) is reduced to

This equation is written in therms of the collisional radiative matrix form for a N total number of populated nl-terms:

$$\begin{pmatrix} \frac{dn_1}{ds} \\ \frac{dn_2}{ds} \\ \vdots \\ \frac{dn_N}{ds} \end{pmatrix} = \begin{pmatrix} C_{1,1} & C_{1,2} & \dots & C_{1,N} \\ C_{2,1} & C_{2,2} & \dots & C_{2,N} \\ \vdots & \vdots & \ddots & \vdots \\ C_{N,1} & C_{N,2} & \dots & C_{N,N} \end{pmatrix} \cdot \begin{pmatrix} n_1 \\ n_2 \\ \vdots \\ n_N \end{pmatrix} + n_{He^+} \begin{pmatrix} R_1^{CX_D,r} \\ R_2^{CX_D,r} \\ \vdots \\ R_N^{CX_D,r} \end{pmatrix} \,.$$

(17)

This system is solved by diagonalizing the CRM matrix, solving the un-coupled first order differential equation, and expressing it in terms of the matrix eigenvalues and eigenvectors:[4,7]

$$n_{nl}(r) = \sum_{\gamma=1}^{N} V_{nl,\gamma} \left\{ \sum_{\iota=1}^{N} V_{\gamma,\iota}^{-1} \left[n_\iota(r_o) e^{\frac{1}{v_n} \lambda_\gamma [r-r_o]} + n_{He^+}(r_o) \frac{R_\iota^{CX_D,r}}{\lambda_\gamma} \left(e^{\frac{1}{v_n} \lambda_\gamma [r-r_o]} - 1 \right) \right] \right\} \,,$$

(18)

where the electron-excitation contribution to the nl-state population is represented by the left-side term inside the brackets, and both CX and recombination contributions are represented by the right-side term inside the brackets. From equation (5), the final solution of the helium neutrals distribution function is given by[7]

$$f_{nl}(\boldsymbol{v}, \boldsymbol{r}, t) = f_o(\boldsymbol{v}) \sum_{\gamma=1}^{N} V_{nl,\gamma} \left\{ \sum_{\iota=1}^{N} V_{\gamma,\iota}^{-1} \left[n_\iota(r_o) e^{\frac{1}{v_n} \lambda_\gamma [r-r_o]} + n_{He^+}(r_o) \frac{R_\iota^{CX_D,r}}{\lambda_\gamma} \left(e^{\frac{1}{v_n} \lambda_\gamma [r-r_o]} - 1 \right) \right] \right\} \,.$$

(19)

III.   BEAM EMISSIVITY ANALYSIS IN AUG

The solution of the kinetic CRM is used to calculate emissivities along the center of a simulated expanding gas-puff injection on the mid-plane for three lines of helium (667.8, 706.5, and 728.1 nm) that are typically used in line-ratio diagnostics.[7] These emissivities are calculated as the gas is injected from the wall into the plasma. The plasma parameters on the mid-plane are obtained from generated 2-D profiles using the EIRENE Monte Carlo transport code.[21] These 2-D profiles are shown in figure 4.

The total deuterium density is calculating by assuming the D_2 molecules are completely dissociated and added to the mono-atomic deuterium. The calculation requires knowledge of the He^+ ion density profiles. In order to estimate these ion profiles, the 1-D kinetic CRM model without recombination and CX is used with the assumption that every ionization will only remain as He^+,[7] and will not undergo a further ionization to He^{2+}. Figure 5 shows the estimated deposited He^+ ion density from the helium gas-puff injection using the plasma profiles along the mid-plane of AUG.
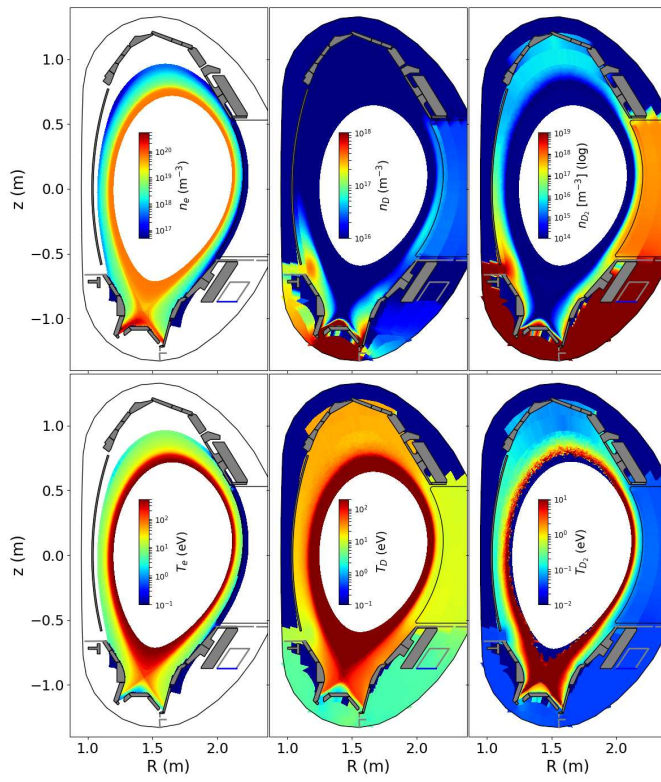
The excited nl-term deuterium populations needed

FIG. 5. Ionization modeling of the helium beam gas-puff as it penerates the plasma.[7] The 1-D kinetic CRM model is used to calculate the density of He$^+$ deposited along the profile as the helium puff gets ionized. This is done in order to quantify both charge-exchange and recombination emission. The figure also includes the plasma parameters from figure 4 projected along the mid-plane of AUG that are used during these calculations, as well as the location of the Last Closed Flux Surface (LCFS).

FIG. 4. Poloidal cross-section of electron and atomic-and molecular neutral deuterium density (upper row) and temperature (lower row) computed by the 3D transport code EMC3-EIRENE[21] for AUG H-mode discharge 30701 at 3.2 s. A separatrix density of 3.2×10^{13} cm^{-3} was assumed at a heating power of 5.2 MW of which 1.6 MW were radiated by impurities.

to quantify the charge-exchange are calculated using a quasi-static equilibrium collisional radiative model that employs state-of-the-art electron-impact excitation RMPS data,[15] and electron-ionization CCC data.[16] This data-set has also been employed in emission calculations from deuterium neutral beam.[22] Figure 6 shows the calculated deuterium ground and excited populations along the mid-plane of AUG.

Both He$^+$ ion and excited deuterium densities from figures 5 and 6 are used to calculate emissivity profiles for electron recombination and and deuterium-He$^+$ CX in order to compare them to the total emissivity as shown by figure 7.

The results from figure 7 clearly show the dominance of the CX emission versus recombination. A direct comparison between the two processes can be clearly made where both electron and deuterium densities are equal (radial location $r = 4\ cm$). It can be appreciated that the contribution from CX to the emission is about 2-orders of magnitude higher than contributions from recombination. The total calculated emissivity that includes
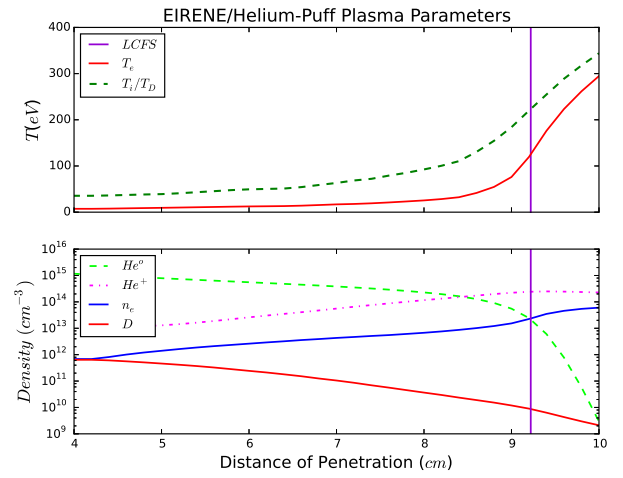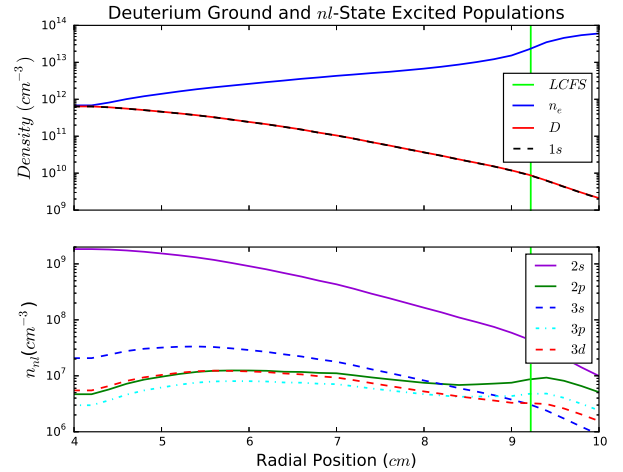

FIG. 6. Calculated deuterium ground and excited population densities along the mid-plane of AUG. The plasma temperatures and densities together with the density of deuterium are used in a quasi-static CRM to calculate the nl-excited population densities that are needed to quantify the charge-exchange emission. Notice that most of the deuterium remains on the ground state while the population of the nl-excited are orders of magnitude lower. The electron density is also included as a base of comparison between CX and recombination, since a direct comparison can be made when $n_e \approx n_D$.

electron-excitation, CX, as well as recombination is also shown.
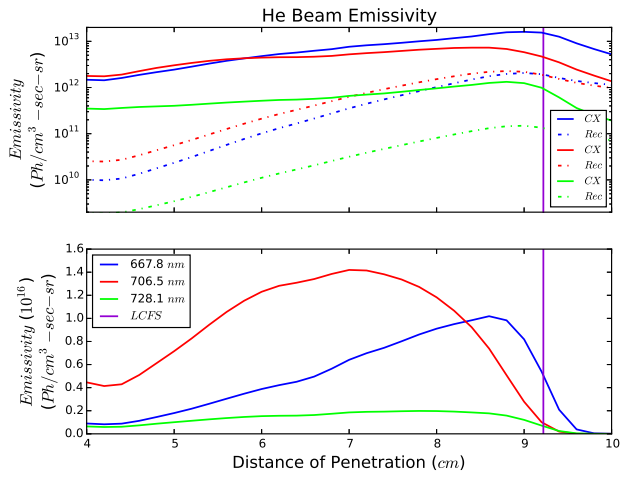
FIG. 7. Calculated electron-recombination and deuterium-He$^+$ charge-exchange emissivities along the mid-plane of AUG. The total emissivity due to electron-excitation is also shown on the botton plot for comparison purposes.

By comparing the results shown in figures 5, 6, and 7 it can be conclude that although CX contributions to the emission are 2-orders of magnitude higher than contributions from recombination, they are still 3-orders of magnitude lower than electron excitation. By looking at the ion/neutral density profiles shown in figure 5, it is clear that while the density of deuterium is higher near the wall and decreases drastically further into the plasma, the He$^+$ ion density is low near the wall and drastically increases further into the plasma. Since deuterium-He$^+$ CX is directly proportional to the product between their densities, the divergent behavior between the two profiles causes the CX emission contributions to be lower than excitation, even though the excited state deuterium cross-sections are 4-orders of magnitude higher than those from the ground state.[10] Another factor that decreases CX emission, is that most of the deuterium is concentrated in the ground state in comparison to the excited population as shown in figure 6.

IV. CHARGE-EXCHANGE AND RECOMBINATION CONTRIBUTION TO ITER LASER-INDUCED FLUORESCENCE

The purpose of the ITER laser-induced fluorescence diagnostic (LIF) is to measure neutral helium densities (n_{HeI}) in the outer leg of the divertor.[26] A laser beam is injected into the plasma and the laser-fluorescent signals are collected through the gap between divertor cassettes (Figure 8). The measurements will be made simultaneously in 24 different spatial locations to provide the n_{HeI} distribution along the laser beam. The LIF will work in conjunction with the divertor Thomson scattering diagnostic (DTS) by employing common laser injection and

signal collection optics.[13] The local electron temperatures and densities (n_e and T_e) in the observation points measured by the DTS[27] will be used to determine n_{HeI} densities from the fluorescent signals using a dynamical collision-radiative model.[5]
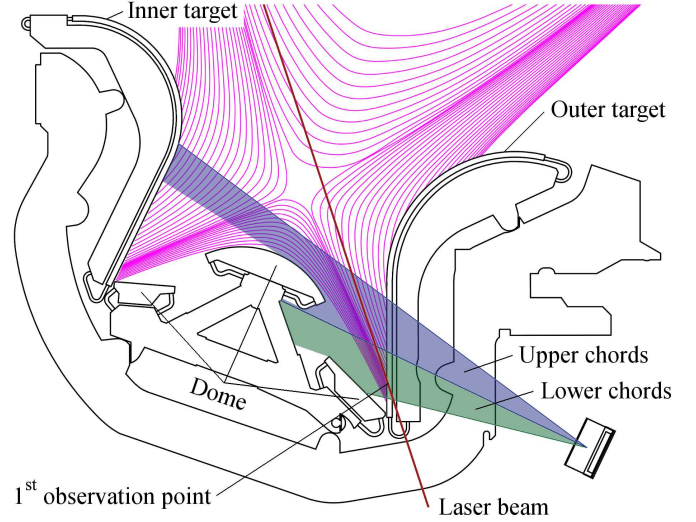

FIG. 8. LIF and DTS diagnostics scheme in ITER.

Spectroscopic schemes for measuring n_{HeI} densities are based on laser excitation of allowed transitions between the metastable singlet 2^1S or triplet 2^3S) state to the 3^1P or 3^3P state (lines 501.6 and 388.9 nm), and the observation of fluorescence in the 3^1D $\rightarrow 2^1$P (667.8 nm) or 3^3D $\rightarrow 2^3$P (587.6 nm) transition (See figure 1). The fluorescent signals depend on the initial populations of the $2^{1,3}$S and $3^{1,3}$P states, as well as the relaxation time of the terms.

SOLPS calculations[28] for ITER #1514(DT) scenarios provide expected plasma parameter distributions (n_e, T_e, n_{HeI}, n_{HeII}, n_{DI}) as a function of poloidal cross-section. The parameters are interpolated into the observation points for this analized scenario (Figure 9). This dataset is used to estimate contributions to both singlet and triplet 2S term populations from charge-exchange and recombination (radiative, 3b, and dielectronic).

Populations of He I $2^{1,3}$S excited states are calculated by assuming quasi-static approximation, and show a strong dominance of charge-exchange and recombination versus electron-impact excitation in the first (lower) observation point (Figure 10). Near the divertor wall, n_{DI} is comparable with n_e, and about three-orders of magnitude higher than n_{HeI}, the electron energy ($T_e \sim 1$ eV) is lower than the threshold energy to excite the atoms from the ground 1^1S ($\Delta E_{1^3S \rightarrow 2^3S} = 19.8$ eV and $\Delta E_{1^1S \rightarrow 2^1S} = 20.6$ eV). Thus, near the wall charge-exchange and recombination processes dominate the emission. In the second observation point, T_e is about 9 eV, which is enough to excite the helium atoms from the ground to the $2^{1,3}$S terms more efficiently than CX and recombination.
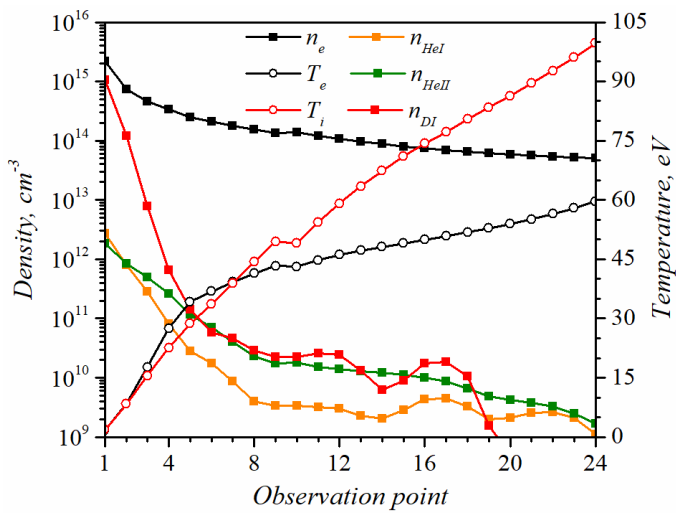
FIG. 9. Plasma parameter distributions along the laser beam interpolated for SOLPS run #1514(DT). The numbering of the observation points is ordered upward from the bottom.
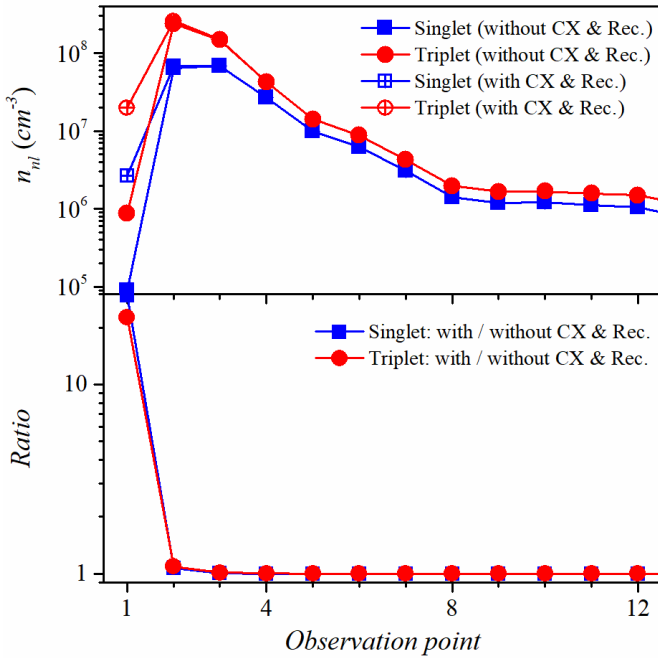

FIG. 10. Populations of the 2^1S and 2^3S states along the laser beam for SOLPS #1514(DT) run with and without considering CX and recombination (top). Ratio of populations between 2^1S and 2^3S states calculated with and without CX and recombination (radiative, 3b, and dielectronic)(bottom).

Contributions of CX and recombination should be taken into account in n_{HeI} measurements near the outer target of the ITER divertor, where T_e is only a few eV. For $T_e > 5$ eV, electron-impact excitation from the ground state dominates over CX and recombination. Therefore, LIF measurements of n_{HeI} in the observation points where $T_e > 5$ eV requires only n_e and T_e values

obtained from DTS, without the need of knowing n_{HeII} and $n_{H,D}$ profiles that are required for CX and recombination calculations.

V. CONCLUSIONS

Recent calculated deuterium-He$^+$ CX cross-sections from excited states have shown to be 4-orders of magnitude larger than those from the ground state.[10] These cross-sections together with electron recombination have been implemented as source terms in a 1-D kinetic collisional radiative model for helium gas-puff into plasma in order to quantify and compare emission contributions from electron-excitation, CX, and recombination.[7,10] Three helium emission lines typically used in diagnostics have been chosen in this analysis (667.8, 706.5, and 728.1 nm).

The results shown in this calculation reveal that although helium emission from charge-exchange is 2-orders of magnitude higher than emission from recombination it is still 3-orders of magnitude weaker than emission from electron excitation. This is due to two main factors: First, although the calculated deuterium density is significantly higher near the wall, most of the population remains in the ground state and only a fraction in the excited states as shown in figure 6. Second, the divergent behavior of both deuterium density and He$^+$ ion along the profile into the plasma. Deuterium densities remain higher near the wall and decrease abruptly by several orders of magnitude to the interior of the plasma, while the He$^+$ ion density shows the opposite behavior where it is very low near the wall, and rapidly increases by several orders of magnitude into the plasma as the helium gas becomes ionized (See figure 5).

Contributions of CX and recombination to LIF diagnostic of helium densities in ITER divertor is negligible for spatial points where electron temperature $T_e > 5$ eV. Based on SOLPS plasma parameter distributions analyzed in this work, only in the nearest observation point to the outer target is where $T_e \sim 1$ eV, and where CX and recombination (radiative, 3b, and dielectronic) are the main populating mechanisms to the 2^1S and 2^3S states where the diagnostic laser pumps from. Electron-impact excitation dominates the population and emission over CX and recombination in the other 23 observation points, and only n_e and T_e values provided by Thomson scattering are required to obtain n_{HeI} profiles from flourescent signals.

It is concluded that due to the small contributions that both CX and electron recombination make, electron-excitation dominates the emission. These results assure confidence on the current line-ratio diagnostic model where electron-excitation emission is assumed to be dominant[4], and recombination effects are eliminated by emission background subtraction.[7,23] However, due to the higher contribution to the neutral helium population that CX makes compared to electron recombination, CX

must be included as an important source in plasma ionic fractional abundance calculations, as well as in helium-ash transport studies in fusion reactors,[24] and helium removal in tokamaks.[25]

ACKNOWLEDGMENTS

[1] O. Schmitz, I. L. Beigman, L. A. Vainshtein, B. Schweer, M. Kantor, A. Pospieszczyk, Y. Xu, M. Krychowlak, M. Lehnen, U. Samm, B. Unterberg, and the TEXTOR Team, Plasma Phys. Control. Fusion **50**, 115004 (2008).

[2] M. Griener, E. Wolfrum, M. Cavedon, R. Dux, V. Rohde, M. Sochor, J. M. Muñoz Burgos, O. Schmitz, U. Stroth, and the AS-DEX Upgrade Team, Rev. Sci. Instrum. **89**, 10D102 (2018).

[3] T. Barbui, M. Krychowiak, R. Koenig, O. Schmitz, J. M. Muñoz Burgos, B. Schweer, A. Terra, and the W7-X Team,, Rev. Sci. Instrum. **87**, 11E554 (2016).

[4] J. M. Muñoz Burgos, O. Schmitz, S. D. Loch, and C. P. Ballance, Phys. of Plasmas **19**, 012501 (2012).

[5] A. V. Gorbunov, D. A. Shuvaev, and I. V. Moskalenko, Plasma Phys. Rep. **38**, 574 (2012).

[6] M. Griener, J. M. Muñoz Burgos, M. Cavedon, G. Birkenmeier, R. Dux, B. Kurzan, O. Schmitz, B. Sieglin, U. Stroth, E. Viezzer, E. Wolfrum, and the ASDEX Upgrade Team, Plasma Phys, Control. Fusion **60**, 025008 (2018).

[7] J. M. Muñoz Burgos, M. Agostini, P. Scarin, D. P. Stotler, E. A. Unterberg, S. D. Loch, O. Schmitz, K. Tritz, and D. Stutman, Phys. of Plasmas **23**, 053302 (2016).

[8] W. Zholobenko, M. Rack, D. Reiter, M. Goto, Y. Feng, B. Küppers, and P. Börner, Nucl. Fusion **58**, 126006 (2018).

[9] J. Loreau, S. Ryabchenko, and N. Vaeck, J. Phys. B: At. Mol. Opt. Phys. **47**, 135204 (2014).

[10] J. Loreau, S. Ryabchenko, J. M. Muñoz Burgos, and N. Vaeck, J. Phys. B: At. Mol. Opt. Phys. **51**, 085205 (2018).

[11] J. Loreau, S. Ryabchenko, A. Dalgarno, and N. Vaeck, Phys. Rev. A **84**, 052720 (2011).

[12] Sh. Azizan, F. Shojaei, and R. Fathi, J. Phys. B: At. Mol. Opt. Phys. **49**, 135201 (2016).

[13] E. E. Mukhin, G. S. Kurskiev, A. V. Gorbunov, D. S. Samsonov, S. Y. Tolstyakov, A. G. Razdobarin, N. A. Babinov, A. N. Bazhenov, E. B. Berik, I. M. Bukreev, P. V. Chernakov, Al. P. Chernakov, An. P. Chernakov, A. M. Dmitriev, D. I. Elets, M. M. Kochergin, A. N. Koval, A. S. Kukushkin, M. G. Levashova, A. E.

Litvinov, V. S. Lisitsa, S. V. Masyukevich, A. N. Mokeev, V. A. Solovei, V. V. Solokha, I. B. Tereschenko, L. A. Varshavchik, K. Y. Vukolov, P. Andrew, M. Kempenaars, G. Vayakis, and M. Walsh, FIP/1-5, FEC (2018)

[14] P. G. Burke and K. A. Berrington "Atomic and Molecular Processes: An R-Matrix Approach," [Institute of Publishing (IOP), Bristol, 1993].

[15] K. Bartschat, Comput. Phys. Commun. **114**, 168 (1998).

[16] I. Bray and A. T. Stelbovics, Phys. Rev. A **46**, 69 (1992).

[17] D. V. Fursa and I. Bray, Phys. Rev. A **52**, 1279 (1995).

[18] Yu. Ralchenko, R. K. Janev, T. Kato, D. V. Fursa, I. Bray, and F. J. de Heer, At. Data Nucl. Data Tables **94**, 603-622 (2008).

[19] V. A. Soukhanovskii, R. Kaita, R. Majeski, and A. L. Roquemore, Rev. Sci. Instrum. **75**, 10D4320 (2004).

[20] W. H. Press, S. A. Teukolsky, W. T. Vetterling, and B. P. Flannery, "Numerical Recipes The Art of Scientific Computing", 3rd Ed. [Cambridge University Press, New York, 2007].

[21] D. Reiter, J. Nucl. Mater. **196-198**, 80-89 (1992).

[22] J. M. Muñoz Burgos, K. H. Burrell, W. M. Solomon, B. A. Grierson, S. D. Loch, C. P. Ballance, and C. Chrystal, Nucl. Fusion **53**, 093012 (2013).

[23] E. A. Unterberg, O. Schmitz, D. H. Fehling, H. Stoschus, C. C. Klepper, J. M. Muñoz-Burgos, G. Van Wassenhove, and D. L. Hillis, Rev. Sci. Instrum. **83**, 10D722 (2012).

[24] M. Jakobs, N. Lopes-Cardozo, and R. Jaspers, Nucl. Fusion **54**, 122005 (2014).

[25] D. Reiter, H. Kever, G. H. Wolf, M. Baelmans, R. Behrisch, and R. Schneider, Plasma Phys. Control. Fusion **33**, 1579 (1991).

[26] A. V. Gorbunov, E. E. Mukhin, E. B. Berik, K. Yu. Vukolov, V. S. Lisitsa, A. S. Kukushkin, M. G. Levashova, R. Barnsley, G. Vayakis, and M. J. Walsh, Fusion Eng. Des. **123**, 695-698 (2017).

[27] E. E. Mukhin, R. A. Pitts, P. Andrew, I. M. Bukreev, P. V. Chernakov, L. Giudicotti, G. Huijsmans, M. M. Kochergin, A. N. Koval, A. S. Kukushkin, G. S. Kurskiev, A. E. Litvinov, S. V. Masyukevich, R. Pasqualotto, A. G. Razdobarin, V. V. Semenov, S. Yu. Tolstyakov, and M. J. Walsh, Nucl. Fusion **54**, 043007 (2014)

[28] H. D. Pacher, A. S. Kukushkin, G. W. Pacher, V. Kotov, R. A. Pitts, and D. Reiter, J. Nucl. Mater. **463**, 591-595 (2015).